Single-Atom Catalysts with Unsaturated Co-N_2 Active Sites Based on a C_2N 2D-Organic Framework for Efficient Sulfur Redox Reaction

Dawei Yang,[†,‡] *Jiaao Wang,*[Δ] *Chenjie Lou,*[◊] *Mengyao Li,*[&] *Chaoqi Zhang,*[‡] *Alberto Ramon,*[‡] *Canhuang Li,*[‡] *Mingxue Tang,*[◊] *Graeme Henkelman,*[Δ] *Ming Xu,*[*,§] *Junshan Li,*[//] *Jordi Llorca,*[$] *Jordi Arbiol,*[±] *David Mitlin,*[*,○] *Guangmin Zhou,*[*,#] *Andreu Cabot*[*,‡,⊥]

[†] Henan Province Key Laboratory of Photovoltaic Materials, School of Future Technology, Henan University, Kaifeng, 475004, P. R. China.

[‡] Catalonia Institute for Energy Research – IREC, Sant Adrià de Besòs, Barcelona, 08930, Spain.

[Δ] Department of Chemistry and the Oden Institute for Computational Engineering and Sciences, The University of Texas at Austin, Austin, TX, 78712 USA.

[◊] Center for High Pressure Science and Technology Advanced Research, Beijing 100193,, P. R. China.

[&] School of Physics and Microelectronics, Zhengzhou University, Zhengzhou 450052, P. R. China.

[§] State Key Laboratory of Chemical Resource Engineering, Beijing University of Chemical Technology, Beijing 100029, P. R. China.

[//] Institute for Advanced Study, Chengdu University, 610106, Chengdu, P. R. China.

[$] Institute of Energy Technologies, Department of Chemical Engineering and Barcelona Research Center in Multiscale Science and Engineering, Universitat Politècnica de Catalunya, EEBE, 08019, Barcelona, Spain.

[±] Catalan Institute of Nanoscience and Nanotechnology (ICN2), CSIC and BIST

Campus UAB, Bellaterra, 08193 Barcelona, Spain.

◦ Materials Science and Engineering Program & Texas Materials Institute, The University of Texas at Austin, Austin, Texas 78712, United States.

Shenzhen Geim Graphene Center, Tsinghua-Berkeley Shenzhen Institute & Tsinghua Shenzhen, International Graduate School, Tsinghua University, Shenzhen, 518055, P. R. China.

⊥ ICREA, Pg. Lluís Companys 23, 08010, Barcelona, Spain.

Email: mingxu@mail.buct.edu.cn

Email: david.mitlin2@utexas.edu

Email: guangminzhou@sz.tsinghua.edu.cn

Email: acabot@irec.cat

Abstract

Lithium-sulfur battery (LSB) is a viable option for the next generation of energy storage systems. However, the shuttle effect of lithium polysulfides (LiPS) and the poor electrical conductivity of sulfur and lithium sulfides limit its deployment. Here, we report on a 2D-organic framework, C_2N, loaded with cobalt single atoms (Co-SAs/C_2N) as an effective sulfur host in LSB cathodes. Experimental results and density functional theory (DFT) calculations reveal that unsaturated Co-N_2 active sites with an asymmetric electron distribution act as effective polysulfide traps, accommodating electrons from polysulfide ions to form strong S_x^{2-}-Co-N bonds. Additionally, charge transfer between LiPS and unsaturated Co-N_2 active sites endows immobilized LiPS with low free energy and low electrochemical decomposition energy barriers,

thus accelerating the kinetic conversion of LiPS during the charge/discharge process. As a result, S@Co-SAs/C_2N-based cathodes exhibit an excellent rate performance with capacities of up to 550 mAh g^{-1} at 10C, impressive cycling stability with over 81% capacity retention over 2500 cycles at 3C, and an areal capacity of 7.2 mAh cm^{-2} under a high sulfur loading of 8.1 mg cm^{-2}, twofold that of commercial lithium-ion batteries. This work highly emphasizes the potential capabilities and promising prospects of single-atom catalysts with unsaturated coordination in LSBs.

Keywords: 2D organic framework (C_2N), Co-N_2 active sites, single-atom catalysts, catalytic conversion, lithium-sulfur batteries

Sulfur has received much attention as a potential cathode material in Li-ion batteries owing to its high theoretical capacity (1672 mAh g^{-1}) and energy density (2600 Wh kg^{-1}), and its low cost and environmental friendliness.[1-3] However, the commercial deployment of lithium-sulfur batteries (LSBs) has been hampered by several limitations. These limitations include the electrical insulating nature of sulfur and lithium sulfide which limits the rate capability and reduces the utilization of active material.[4,5] Besides, the lithium polysulfides (LiPS) formed during the electrochemical S_8-Li_2S redox reaction are soluble in conventional organic electrolytes and can migrate to the anode. This LiPS shuttle effect reduces the energy efficiency of the charge-discharge process, decreases the cathode active material, and corrodes the lithium anode, which results in irreversible capacity degradation. Therefore, strategies to promote charge transport at the cathode, immobilize the LiPS, and facilitate their reaction kinetics are highly desired.[6,7]

One effective approach to overcome some of these challenges is to combine sulfur with high surface area and porous carbon-based materials to increase the cathode electrical conductivity and at the same time confine the LiPS.[8-10] However, the weak interaction between nonpolar carbon and polar LiPS prevents fully suppressing their dissolution and migration. On the other hand, some polar inorganic materials showing strong chemical interaction with polysulfides have been proposed to more effectively anchor and confine LiPS.[11-13] However, even when strongly bound to a cathode additive, the sluggish conversion kinetics of adsorbed LiPS results in an accumulation of LiPS that are eventually released into the solution. Thus, in addition to large surface area conductive additives and mechanisms for trapping LiPS, the integration of electrocatalysts able to facilitate the LiPS redox reactions is required.

Carbon-supported single-atom catalysts (SACs), which are gaining great momentum in the field of electrocatalysis due to their high activities with almost 100% atomic utilization and excellent electrical conductivities, are an excellent candidate to overcome the kinetic limitations of the Li-S reaction.[14-17] In addition, some SACs also exhibit high sulfiphilicity, which enables them to contribute to the immobilization of LiPS. The electrocatalytic activity of SACs strongly depends on the metal local environment, which is determined by the local coordination configuration.[18] M-N_4 moieties (M = Fe, Co, Ni, etc.) are the active sites of the commonly reported SACs.[19-21] SACs with M-N_4 moieties afford symmetrical electron distributions, which limits the adsorption and activation of reaction intermediates, thus its catalytic performance.[22,23] Improved performances can be obtained with the asymmetrical electron distribution of M-N_x ($x\neq4$) coordination structures. While these electrocatalytic moieties have been previously tested,[15] there is a lack of understanding of the relationship between the electronic structure of M-N_x SACs and electrocatalytic performance towards LiPS conversion.

Aside from the metal moiety, the carbon support also influences the electrocatalytic performance. Two-dimensional (2D) carbon supports with high specific surface area and lamellar structure can accommodate a massive density of SAC active sites. Recently, C_2N has sparked significant interest as a novel 2D graphene-like covalent organic framework (COF) characterized by a huge specific surface area and effective charge transfer.[24] C_2N consists of a uniform porous structure with hollow sites surrounded by six pyridine nitrogen atoms (N_6 cavities) that provide a large number of effective sites for the coordination of a high density of single metal atoms.[25-27] Within this framework, the diffusion barrier of metal atoms is too high to form aggregates. These properties make C_2N an excellent support for the rational design and

engineering of single-atomic mediators with asymmetrical electron distribution to improve the electrochemical performance of LSBs.

In this work, we detail the synthesis of dispersed Co single atoms supported on C_2N (Co-SAs/C_2N) with a Co-N_2 coordination structure through a pyrolysis-free wet-chemistry strategy. The unsaturated Co-N_2 sites can not only provide strong LiPS adsorption capacity to suppress the shuttle effect but also promote interfacial charge transfer to accelerate the redox kinetics of the LiPS. Benefiting from the simultaneous optimization of the carbon support and the SACs coordination environment, Co-SAs/C_2N exhibits excellent electrocatalytic activity that enables bidirectional sulfur redox chemistry, accelerating the precipitation/decomposition of Li_2S and lowering the related energy barriers. The performance of S@Co-SAs/C_2N cathodes is thoroughly tested to demonstrate their superior cycling stability and rate capability. The outstanding obtained results are rationalized with the help of density functional theory (DFT) calculations.

RESULTS AND DISCUSSION

A scalable wet-chemistry strategy was designed for the synthesis of C_2N-supported Co-based SACs, as displayed in Figure 1a. Briefly, Co^{2+} was coordinated with nitrogen atoms from hexaaminobenzene (HAB) to form the Co-HAB complex. Subsequently, Co-HAB was polymerized and reduced in the presence of chloranilic acid to form Co-SAs/C_2N. The targeted material should have a periodic conjugated ring structure with Co ions confined in the C_2N pores.

Scanning electron microscopy (SEM) analysis showed Co-SAs/C_2N to display a stacked-layered structure (Figure S1a). According to energy-dispersive X-ray spectroscopy (EDX) results, the N/Co atomic ratio of Co-SAs/C_2N is *ca.* 2, which corresponds to an average of one Co^{2+} ion every two N sites in C_2N (Figure S1b). Inductively coupled plasma optical emission spectroscopy (ICP-OES) determined the Co loading in the Co-SAs/C_2N to be 12.8%. This high metal loading, above that generally reported SACs (Table S1), is enabled by the high density of anchoring sites and pores in C_2N.

Aberration-corrected high-angle annular dark-field scanning transmission electron microscopy (AC HAADF-STEM) analysis showed no cobalt nanoparticles/clusters anywhere around the Co-SAs/C_2N sample (Figure 1b). In contrast, as highlighted with red circles in Figure 1c,d, a large number of highly dispersed bright spots, identified as Co atoms, were observed within the C_2N skeleton. EDX elemental mapping demonstrated C, N, and Co to be homogenously distributed within Co-SAs/C_2N (Figure 1e). X-ray diffraction (XRD) patterns of the as-synthesized Co-SAs/C_2N show a main broad diffraction peak at about 26.5°, corresponding to the (002) plane of C_2N (Figure S2). In addition, no diffraction peaks related to Co-based compounds were detected, indicating that Co atoms are most likely uniformly and atomically dispersed within the C_2N matrix, which is consistent with the AC HAADF-STEM analysis.

The same synthesis strategy can be used to produce Ni-SAs/C_2N and Fe-SAs/C_2N, using $NiCl_2 \cdot 6H_2O$ (4.5 mmol) and $FeCl_3 \cdot 6H_2O$ (4.5 mmol) as metal precursors, respectively. Figure S3 displays the XRD pattern of the materials, showing no peak related to Ni- or Fe-based phases while EDX analysis detects relatively high amounts of highly distributed metal in both materials.

To reveal the elemental composition and chemical bonding states of Co-SAs/C_2N, X-ray photoelectron spectroscopy (XPS) spectra were measured. As shown in the survey XPS spectrum displayed in Figure S4a, Co, C, N, and O elements were identified. The high-resolution C 1s spectrum was fitted using three bands (Figure S4b), with the main one, at 284.6 eV, being associated with C-C/C=C bonds.[12,28] The high-resolution N 1s XPS spectrum was fitted with four bands at 398.9 eV, 401.2 eV, 402.3 eV, and 399.8 eV, corresponding to pyridinic-N, pyrrolic-N, graphitic-N, and Co-N bonds,[29,30] respectively (Figure S4c). In the Co 2p XPS spectrum (Figure S4d), besides the satellite peaks, a single doublet at 781.3 eV and 797.5 eV pointed at the existence of Co within a Co^{2+} chemical environment.[9,31]

X-ray absorption near-edge structure (XANES) measurements of the Co K-edge were used to further reveal the chemical structure of Co-SAs/C_2N and particularly the valence state of Co, using a cobalt phthalocyanine (CoPc) and Co foil as references (Figure 2a, Table S2). The Co K-edge XANES profile indicates that the Co atoms in Co-SAs/C_2N are at a higher oxidation state than those of CoPc and Co foil, which is compatible with a Co-N_2 coordination.[32,33] The absorption edge further indicated that the Co coordination environment is compatible with Co-N_2 bonds within the C_2N structure.

Figure 2b shows the Fourier-transformed extended X-ray absorption fine structure (FT-EXAFS) spectrum of Co-SAs/C_2N, which displayed a peak at ~1.62 Å that could be identified as Co-N scattering paths. This result is again compatible with Co atoms being coordinated with N within the C_2N support. Notice also that the Co-Co peak at ~2.25 Å observed in the Co foil was not observed in the Co-SAs/C_2N spectrum, again suggesting that isolated Co atoms were anchored on the C_2N matrix by Co-N coordination.[34,35]

From the fitting of the EXAFS spectra at the Co K-edge (Figure 2c), the average coordination number of Co atoms within Co-SAs/C_2N was ~2.2 (Table S2). Thus, on average, each Co atom is coordinated with two N atoms to form Co-N_2 sites. The atomic structure model of Co-SAs/C_2N is displayed as an inset in Figure 2c. The oscillation curve of Co-SAs/C_2N was clearly distinct from that of CoPc and Co foil, again suggesting the coordination of Co to N atoms (Figure 2d).

The wavelet transform (WT) of the Co K-edge spectrum was employed to further demonstrate the bonding environment of Co species (Figure 2e-g). Compared with CoPc and Co foil, one prominent intensity maximum can be found at around 4.68 $Å^{-1}$, which belongs to the Co-N scattering path in the Co-SAs/C_2N WT contour plot without observable Co-Co contribution.[36] This result further confirms the particular Co-N coordination environment at Co sites as well as the single-atom configurations in Co-SAs/C_2N. The atomic structure model of the Co-SAs/C_2N is displayed in Figure 2h.

The solid-state ^{13}C magic-angle-spinning (MAS) nuclear magnetic resonance (NMR) spectrum of Co-SAs/C_2N is shown in Figure 2i. The resonance signal of Co-SAs/C_2N is centered at around 150 ppm with a very broad distribution, indicating the carbon atoms of the phenyl edges connected to C=C units and the carbon atoms of triphenylene cores on vertices with intensive rigidity.[12] Besides, the continuous wave electron paramagnetic resonance (CW-EPR) signal at a g-value of 2.004 confirmed the presence of abundant defects with unpaired electrons in Co-SAs/C_2N (Figure 2j).

For a deeper exploration of the electronic structure of Co-SAs/C_2N, DFT calculations were performed. As shown in Figure S5, the electronic band structure of Co-SAs/C_2N obtained from

the DFT calculations within the HSE06 functional showed several bands crossing the Fermi level, demonstrating that the cobalt atoms doping could improve the intrinsic conductivity of the C_2N matrix.[12,37] To experimentally determine this electrical conductivity, we performed 4-point measurements of the material based on the four-point probe method. As displayed in Figure S6, experimentally, Co-SAs/C_2N showed a significantly higher electrical conductivity of 196.7 S cm^{-1}, nearly sixfold above that of C_2N of 32.6 S cm^{-1}. This improved electrical conductivity should promote the electrochemical properties of the material.

To analyze the electrochemical performance of Co-SAs/C_2N as a sulfur host in LSBs, sulfur was introduced within the Co-SAs/C_2N by a melt-diffusion process. SEM-EDX characterization of the obtained S@Co-SAs/C_2N composites confirmed the presence of S homogeneously distributed within the host material (Figure S7a). XRD patterns further showed the presence of crystalline sulfur (JCPDS No. 08-0247) within S@Co-SAs/C_2N (Figure S7b).[38] The sulfur content was quantified at about 70.2 wt% by thermogravimetric analysis (TGA) (Figures S8 and S9). Besides, with the introduction of sulfur, the Brunauer–Emmett–Teller (BET) specific surface area of the material sharply decreased from 189.6 $m^2\ g^{-1}$ (Co-SAs/C_2N) to 11.5 $m^2\ g^{-1}$ (S@Co-SAs/C_2N), as shown in Figure S10. Moreover, four-point probe measurements showed the electrical conductivities of S@Co-SAs/C_2N (20.5 S cm^{-1}) to be nearly fivefold larger than that of S@C_2N (3.8 S cm^{-1}). These results overall confirm that sulfur was incorporated into the Co-SAs/C_2N catalytic host.

To evaluate the LiPS adsorption ability of the host material, a certain amount of Co-SAs/C_2N and C_2N were immersed in separate vials containing the same 1×10^{-2} M Li_2S_4 solution. After overnight adsorption, clear differences in the color of the solution containing the different

materials were observed. The color of the Li_2S_4 solution containing Co-SAs/C_2N was much lighter than that of the solution containing C_2N (light yellow), indicating the former has a much higher LiPS adsorption ability. This result was further confirmed using UV-vis spectroscopy (Figure 3a),[18,39] showing the UV-vis absorption associated with the presence of the polysulfide, at 300-500 nm, to be much more strongly reduced in the presence of Co-SAs/C_2N than with C_2N.

Figure 3b shows the N 1s XPS spectra of Co-SAs/C_2N before and after Li_2S_4 adsorption. The N 1s spectrum of the sample Li_2S_4 adsorption is shifted towards lower binding energy (BE), which is related to a higher electronic density associated with the binding of the N atoms in C_2N, having a Lewis base character, with Li atoms in Li_2S_4, having a Lewis acid character.[40,41] The formation of Li-N bonds was also confirmed by analyzing the Li 1s spectrum, which besides the Li-S peak related to Li_2S_4, also displays a Li-N contribution at 56.4 eV (Figure S11a).[42]

Figure 3c exhibits the high-resolution Co 3d XPS spectrum of Co-SAs/C_2N and Co-SAs/C_2N-Li_2S_4. Compared with the original Co 3d spectrum, after Li_2S_4 adsorption, the Co 3d spectrum shifted to higher binding energies, which is likely due to the chemical interaction between Co and sulfur, forming Co-S bonds.[27,43] In addition, the S 2p XPS spectrum of Co-SAs/C_2N-Li_2S_4 is depicted in Figure S11b. As described in the literature, the S 2p XPS spectrum of Li_2S_4 displays two doublets, the main one located at a binding energy of 163.2 eV (S $2p_{3/2}$) and attributed to the central bridging sulfur atom (S_B^0), and a minor one at 161.6 eV (S $2p_{3/2}$) corresponds to the terminal sulfur (S_T^{-1}).[11] In contrast to the spectrum of pure Li_2S_4, Co-SAs/C_2N-Li_2S_4 exhibited two higher binding energy contributions at 163.6 and 162.9 eV,

representing +0.4 and +0.3 eV shifts for S_B and S_T, respectively. The shifts arise from the polarization of electrons away from the sulfur atoms to the electropositive Co atom at the interface, confirming the formation of a Co-S bond.[23,40]

To further study the interactions between Co-SAs/C_2N and polysulfides, the ^{7}Li NMR spectrum of Li_2S_4 before and after interacting with Co-SAs/C_2N were collected and displayed in Figure 3d.e. Because the chemical shift is quite sensitive to the surrounding environment, the changed chemical shift thus concurrently corresponds to the strong binding between Li_2S_4 and Co-SAs/C_2N. The pure Li_2S_4 shows a single peak at 0 ppm with a sharp signal, which becomes broader when attached to Co-SAs/C_2N. An additional broad signal appears at around -5 ppm, which is possibly due to the strong shielding effect caused by the Co-SAs/C_2N rings. According to the above analysis and ^{7}Li NMR experiments on Co-SAs/C_2N-Li_2S_4 model system, a series of insights can be subtracted: 1) Co-SAs/C_2N has strong binding to Li_2S_4 as suggested by the high binding energy; 2) a dipole-dipole interaction, namely Li bond, forms between Li_2S_4 and Co-SAs/C_2N to afford the strong binding; 3) the formation of Li-N bond alters the local environment surrounding Li, resulting in a shift in the NMR spectrum.

The interactions between Li_2S_4 and Co-SAs/C_2N were further confirmed by CW-EPR characterizations. As shown in Figure 3f, a decrease in EPR signal intensity was obtained with the Li_2S_4 adsorption, i.e. when comparing the EPR spectrum of Co-SAs/C_2N and Co-SAs/C_2N-Li_2S_4. This lower EPR signal denotes a decrease in the density of unpaired electrons, which implies that the sites with unpaired electrons, e.g. carbon vacancies, serve as active sites for the adsorption of LiPS.

DFT calculations were performed to further evaluate the interaction between LiPS and Co-SAs/C_2N. Figures S12 and S13 exhibit the optimized adsorption configuration of LiPS species on C_2N and Co-SAs/C_2N at six different lithiation stages (Li_2S, Li_2S_2, Li_2S_4, Li_2S_6, Li_2S_8 and S_8). The Li and S atoms of Li_2S_x species can form chemical bonds with N and Co atoms in C_2N and Co-SAs/C_2N, respectively, attributed to the coupling between Lewis acids (Li and Co atoms with unoccupied orbitals) and Lewis bases (N and S atoms with lone electron pairs).[12,44] As shown in Figure 3g, the calculated BE (E_b) of Li_2S_4 on C_2N and Co-SAs/C_2N surfaces were -2.49 eV and -6.61 eV, respectively, which endows Co-N_2 sites with enhanced adsorption ability for Li_2S_4. Actually, all the LiPS species showed higher affinity for the Co-SAs/C_2N surface rather than for the C_2N one (Figure 3h). These results suggest robust chemisorption of LiPS on Co-SAs/C_2N, which should block the LiPS shuttle effect.

To reveal the electrocatalytic activity of Co-SAs/C_2N for polysulfide conversion, CV measurements were initially performed on symmetric cells containing a Li_2S_6 electrolyte within a voltage window of -0.8 to 0.8 V (Figure 4a). The Co-SAs/C_2N-based cell displayed two symmetric cathodic/anodic peaks, which were associated with the electrochemical oxidation/reduction of Li_2S_6:[38,45]

$$S_6^{2-} + 10e^- + 12Li^+ \leftrightarrow 6Li_2S \quad (1)$$

$$4S_6^{2-} \leftrightarrow 8e^- + 3S_8 \quad (2)$$

The cell containing Co-SAs/C_2N electrodes provided higher currents compared with the C_2N-based cell, indicating the superior catalytic activity of Co-SAs/C_2N toward the liquid-solid redox reaction ($Li_2S \leftrightarrow S_6^{2-} \leftrightarrow S_8$). Besides, Co-SAs/$C_2N$ electrodes displayed quasi-rectangular CV curves, pointing toward a pure capacitive behavior (Figure S14a).[43,46] The CV

curves retained their shape after undergoing 20 cycles, pointing to an excellent stability of the Co-SAs/C_2N electrodes (Figure S14b).

The CV curves of Li-S coin cells based on S@Co-SAs/C_2N and S@C2N cathodes are shown in Figure 4b. The cathodic peak voltage (peak I) is associated with the reactions:[12,47]

$$S_8 + 2e + {}^{-}2\mathrm{Li} \rightarrow {}^{+}\mathrm{Li}_2S_8$$

$$3Li_2S_8 + 2e^- + 2Li^+ \rightarrow 4Li_2S_6$$

$$2Li_2S_6 + 2e^- + 2Li^+ \rightarrow 3Li_2S_4$$

The cathodic peak (peak II) corresponded to the reactions:

$$Li_2S_4 + 2e^- + 2Li^+ \rightarrow 2Li_2S_2$$

$$Li_2S_2 + 2e^- + 2Li^+ \rightarrow 2Li_2S$$

The anodic peak (peak III) accounts for the reverse multistep oxidation process of short-chain sulfides to LiPS and eventually to sulfur.[18,48] S@Co-SAs/C_2N electrodes exhibited much higher peak currents and the cathodic/anodic peaks located at more positive/negative potentials than S@C_2N, demonstrating that Co-SAs/C_2N was the most effective catalyst in promoting the polysulfides redox reaction kinetics (Figure4 b,c). The catalytic activity of Co-SAs/C_2N electrodes was quantified through the onset potential at a current density of 10 μA cm^{-2} beyond the baseline current (Figure S15, 4c).[38,49] The cells based on S@Co-SAs/C_2N electrodes were characterized by higher/lower onset potentials for cathodic/anodic peaks, demonstrating faster redox kinetics for the LiPS conversion reaction.

The electrocatalytic activity of Co-SAs/C_2N-based electrodes was further analyzed by measuring CV at various scan rates, from 0.1 to 0.4 mV s^{-1} (Figure 4d). With the increase in the scan rate, S@Co-SAs/C_2N-based cells displayed higher redox peak currents and lower

polarization potentials compared with S@C_2N-based cells (Figure S16). Notably, the CV curves measured from S@Co-SAs/C_2N cathodes almost overlapped during the first three cycles, indicating good reversibility of the sulfur redox reactions (Figure S17).

The cathodic/anodic peak currents showed a linear relationship with the square root of the scanning rates, pointing at a diffusion-limited reaction. Therefore, the Randles-Sevcik equation was used to calculate the diffusion constant of lithium ions (D_{Li+}) in the process:[50,51]

$$I_{\mathrm{p}} = (2.69*10^5)n^{1.5}AD_{Li^+}{}^{0.5}C_{Li^+}v^{0.5}$$

Where I_p is the peak current, n represents the number of charge transfer, A is the geometric electrode area, C_{Li+} is the concentration of Li^+, and v is the scan rate. A, n, and C_{Li+} are constant in this equation, thus the sharper $I_p/v^{0.5}$ slopes, the faster Li^+ diffusion. As plotted in Figure S18, compared with S@C_2N, S@Co-SAs/C_2N electrodes exhibited the sharpest slopes among the three peaks, thus the highest Li^+ diffusivity during the redox reactions. In peak I, II, and III, S@Co-SAs/C_2N electrodes were characterized by D_{Li+} of 3.67×10^{-7}, 5.94×10^{-7}, and 7.53×10^{-7} cm^2 s^{-1}, respectively, significantly higher than those of S@C_2N (Figure 4e), consistent with the higher reaction kinetics measured. DFT calculations revealed this higher Li+ diffusivity to be related to the decrease of the lithium-ion diffusion barrier on the C_2N surface by the introduction of cobalt atoms (Figure S19).

The galvanostatic charge/discharge profiles for S@Co-SAs/C_2N and S@C_2N electrodes at a current rate of 0.1 C are displayed in Figure 4f. All electrodes show one charge plateau and two discharge plateaus, consistently with the measured CV results associated with the multistep sulfur reaction mechanism. The voltage gap ΔE between the oxidation and the second reduction plateaus is taken as the polarization potential.[46,52] S@Co-SAs/C_2N electrodes were

characterized by significantly lower polarization potentials (ΔE = 126 mV) than S@C_2N electrodes (ΔE = 168 mV) (Figure 4g), confirming the superior catalytic activity of Co-SAs/C_2N toward LiPS conversion.

The catalytic activity of the host materials toward the LiPS conversion reaction was also quantified by the ratio Q2/Q1, where Q1 is the capacity of the first discharge plateaus corresponding to the reduction of sulfur to soluble LiPS ($S_8 + 4Li^+ + 4e^- \rightarrow 2Li_2S_4$) and Q2 is the capacity of the second discharge plateaus corresponding to the subsequent reduction to insoluble sulfide ($2Li_2S_4 + 12Li^+ + 12e^- \rightarrow 8Li_2S$).[43,53] The higher the Q2/Q1 value, the superior the catalytic ability. S@Co-SAs/C_2N electrodes exhibited the highest Q2/Q1 ratio at 2.62, close to the theoretical value (Q2/Q1 = 3) and well above that of S@C_2N (1.99), which further evidences the superior catalytic properties of Co-SAs/C_2N with unsaturated Co-N_2 active sites towards LiPS redox reaction.

Electrochemical kinetics were further assessed in the phase conversion between the soluble LiPS and insoluble Li_2S_2/Li_2S during the charge/discharge processes. There existed a voltage jump at the initial discharging period associated with the Li_2S activation overpotentials.[34] As shown in Figure 4h, S@Co-SAs/C_2N electrodes exhibit a significantly lower overpotential than S@C_2N electrodes. In addition, the galvanostatic charge curves displayed a voltage dip at the beginning of the initial charging period, corresponding to the overpotential of the Li_2S oxidation process (Figure S20).[46] Compared with S@C_2N electrodes, S@Co-SAs/C_2N electrodes displayed a lower Li_2S oxidation overpotential, demonstrating a promoted Li_2S dissolution.

To further assess the catalytic activity of the electrode materials on the reversible reaction between polysulfide molecules and solid Li_2S_2/Li_2S, potentiostatic nucleation experiments were

performed. Based on Faraday's law and the potentiostatic discharge profiles in Figure 4i, S@Co-SAs/C_2N electrodes showed faster responsivity toward Li_2S nucleation and higher capacity of Li_2S precipitation (283.6 mAh g^{-1}) than S@C_2N electrodes (192.1 mA h g^{-1}). This result further proved that Co-SAs/C_2N with unsaturated Co-N_2 active sites significantly reduces the energy barrier of the Li_2S nucleation, enhancing the Li_2S precipitation kinetics.[16,54]

DFT calculations were further used to evaluate the reaction kinetics of the charging process on the surfaces of C_2N and Co-SAs/C_2N. The initial, transition, and final states of Li_2S decomposition on C_2N and Co-SAs/C_2N are displayed in Figures S21 and S22. As shown in Figure 4j, the energy barrier of Li_2S decomposition on Co-SAs/C_2N is only 0.88 eV, much lower than on C_2N (1.25 eV). This result points to Li_2S being much more easily oxidized into LiPS on the Co-SAs/C_2N surface than on C_2N during charging, leading to improved redox reversibility between Li_2S and LiPS and enhanced S utilization.[10,55]

The Gibbs free energies of the main reduction products (S_8, Li_2S_8, Li_2S_6, Li_2S_4, Li_2S_2, and Li_2S) with optimized structures on C_2N and Co-SAs/C_2N are displayed in Figure 4k. Generally, the highest increase of Gibbs free energy (ΔE) is obtained for the reduction of Li_2S_2 to Li_2S, which is considered the rate-limiting step in LSBs.[34,56] As shown in Figure 4k, Co-SAs/C_2N provided a much lower ΔE (0.56 eV) than C_2N (0.79 eV), further confirming that the reduction of S is more thermodynamically favorable on the former.

The galvanostatic charge/discharge profiles of S@Co-SAs/C_2N at different current rates are exhibited in Figure 5a. All discharge curves displayed two well-defined discharge plateaus, even at the highest current density of 10 C. In contrast, S@C_2N electrodes showed a high polarization potential and low capacity response (Figure S23). Figure 5b shows the rate

performances of the cells based on the two electrodes tested, at current rates from 0.2 to 10 C. S@Co-SAs/C_2N electrodes were characterized by an ultrahigh initial discharge capacity of 1415 mA h g^1 at 0.2 C, pointing toward an optimized sulfur activity and utilization. Even at the highest current rate of 10 C, an average capacity of 556 mAh g^{-1} was stabilized, well above the capacity obtained for S@C_2N electrodes. It is worth mentioning that when switched back the current rate to 0.5 C, the average capacity of the cells with S@Co-SAs/C_2N electrodes returned to ≈ 1066 mAh g^{-1}, suggesting remarkable reversibility and stability.

The LSBs energy conversion efficiency during the charge/discharge process was calculated by the ratio of energy output/input:[27,57]

$$E = \int UIdt$$

As exhibited in Figure 5c, S@Co-SAs/C_2N electrodes displayed energy efficiencies around 92.1% at 0.2 C, well above that of S@C_2N electrodes. When the current rate increased to 10 C, S@Co-SAs/C_2N electrodes were characterized by a higher energy efficiency of 80.3% at 10 C than S@C_2N electrodes (63.6%). We associate this higher energy efficiency with the lower polarization potential, which was related to the excellent catalytic effect of Co-SAs/C_2N with unsaturated Co-N_2 active sites.

Figure 5d displays the cycling tests of different cells based on S@Co-SAs/C_2N and S@C_2N cathodes at 0.5 C. S@Co-SAs/C_2N electrodes delivered an initial discharge capacity of 1118.6 mAh g^{-1} and still maintained a stable capacity of 1066.2 mAh g^{-1} after 100 cycles. For comparison, the discharge capacity of the S@C_2N electrodes decayed to 676.5 mAh g^{-1} after 100 cycles with a capacity loss of 7.5%.

Electrochemical impedance spectroscopy (EIS) was used to further understand the parameters behind the enhanced redox kinetics of S@Co-SAs/C_2N electrodes. Figures 5e and S24 show the Nyquist plot of the EIS spectra obtained from S@Co-SAs/C_2N and S@C_2N coin cells before and after cycling at 0.5 C. The fresh electrodes display a semicircle at the high-frequency range related to the charge transfer resistance (R_{ct}), and a sloping straight line at lower frequencies related to the lithium ions diffusion.[43] After cycling, a new additional semicircle in the high-frequency region was ascribed to the precipitation of the insulating discharge products of Li_2S on the electrode surface (R_p),[46] and the second semicircle in the middle-frequency region corresponded to the R_{ct}. The S@Co-SAs/C_2N electrodes were characterized by a considerably lower R_p and R_{ct} compared with S@C_2N electrodes after cycling (Table S3). The small R_p value obtained for Co-SAs/C_2N hosts was associated with a reduction of the deposition of insulting Li_2S/Li_2S_2 on the surface, indicating improved electrode kinetics.

Additional cycling was carried out on the S@Co-SAs/C_2N electrodes at a current rate of 1 C (Figure 5f). After 1000 cycles, S@Co-SAs/C_2N electrodes still delivered a discharge capacity of 945.5 mAh g^{-1}, showing an average 0.010% decay per cycle and a stable and high Coulombic efficiency above 99.5%. Besides, an ultra-long cycling test was performed for the S@Co-SAs/C_2N-based cathode at a higher current density of 3 C to evaluate the cycling stability of the host materials (Figure 5g). The S@Co-SAs/C_2N electrode provided an initial discharge capacity at 3 C of 826 mAh g^{-1} and it retained 80.9% of its capacity after 2500 cycles, indicating a low capacity decay rate of just 0.008% per cycle. This decay rate was well below that of the S@C_2N electrodes, which retained 59.8% of its initial capacity after 1000 cycles at 3 C (Figure S25).

To achieve high energy density LSBs that satisfy practical applications, increasing the areal sulfur loading and decreasing the amount of electrolyte are fundamental.[58] Figure 5h shows the high-loading performance of the S@Co-SAs/C_2N electrodes at a sulfur loading of 3.0, 5.2, and 8.1 mg cm^{-2} at 0.2 C, and an electrolyte-to-sulfur (E/S) ratio of 8.9, 6.1, and 4.7 μL mg^{-1}, respectively. High areal capacities of 3.69, 4.64, and 6.32 mAh cm^{-2} after 100 cycles can be obtained under the sulfur loading of 3.0, 5.2, and 8.1 mg cm^{-2}, respectively. Figure S26 shows a series of electrochemical tests of S@Co-SAs/C_2N electrodes with different sulfur loadings. Galvanostatic charge/discharge curves of S@Co-SAs/C_2N electrodes showed clear charge/discharge plateaus at the various current rates tested. S@Co-SAs/C_2N electrodes displayed stable charge/discharge curves and delivered a high areal capacity of 7.18 mAh cm^{-2} under raised sulfur loading of 8.1 mg cm^{-2}, which is almost a twofold of that of commercial Li-ion batteries (4 mAh cm^{-2}). This excellent performance at a high sulfur loading confirmed the good reaction kinetics that is attributed to the superior catalytic activity of the unsaturated Co-N_2 sites of Co-SAs/C_2N.

Figure S27 shows SEM images of the S@Co-SAs/C_2N cathodes with a high S loading after cycling, showing no cracks being developed. The excellent mechanical stability of the material is related to the high porosity of the host material Co-SAs/C_2N that can accommodate the volume changes during cycling. The experimental density of the films was determined from their thickness and weight at 1.27 g/cm^3. Taking into account the 70% sulfur loading measured by TGA, the relative density of the film was estimated at 60%. Taking into account the 80% volume change in the conversion of S into Li_2S, an increase of relative density from 60% to

92% is to be expected during the discharging process. Thus the porosity is high enough for the volume expansion to fill the voids without representing a major volume change of the film.

To further demonstrate the important role played by Co in the superior material performance, additional samples with a lower Co amount were produced and tested. Figure S28 shows the cycling performance at 1 C over 500 cycles of a S@Co-SAs/C_2N electrode based on a Co-SAs/C_2N SAC containing just a 3.2 wt% of Co. As expected, the performance of this sample was sensibly lower than that of the sample containing a higher Co amount but improved with respect to the sample containing no Co.

The electrochemical results of S@Co-SAs/C_2N cathodes for LSBs are compared to other state-of-the-art single atoms-based materials in Table S4 (Supporting Information). Overall, S@Co-SAs/C_2N electrodes were characterized by an excellent electrochemical performance related to the following properties: 1) The abundance of different types of nitrogen and pores in the C_2N structure, which capture LiPS and suppress the shuttle effect; 2) The high electrical conductivity of Co-SAs/C_2N that maximizes the sulfur utilization; 3) The presence of the unsaturated Co-N_2 sites, which work as efficient catalytically active sites to simultaneously immobilize LiPS and accelerate their redox conversion; and 4) The high catalyst content offering a large density of adsorption/reaction sites enabled by the high nitrogen and pore density of C_2N. All these results indicate that S@Co-SAs/C_2N electrodes can definitively help LSBs to reach practical applications.

CONCLUSIONS

In summary, the synthesis of Co-SAs/C_2N with a precise Co-N_2 coordination structure and its use to explore the adsorption and catalytic properties of Co-N_2 sites in the conversion process of LiPS have been described. Co-SAs/C_2N exhibits lithiophilic/sulfiphilic binding with polysulfides to prevent the dissolution of LiPS into the electrolyte. Besides, within this structure, the unsaturated Co-N_2 center can act as a multifunctional site for accelerating the redox conversion of LiPS and reducing the reaction energy barrier of Li_2S deposition and decomposition during discharge/charge processes, as determined by X-ray absorption fine spectroscopy, experiments and DFT calculations. As a result, S@Co-SAs/C_2N cathodes delivered a more exciting rate performance up to 10 C and an impressive ultra-long-term cycling stability with a negligible capacity decay of 0.008% per cycle over 2500 cycles. More significantly, even at high sulfur loadings and lean electrolyte conditions, S@Co-SAs/C_2N cathodes displayed a remarkable areal capacity meeting the demands of commercial LIBs (4 mAh cm^{-2}). This work sheds light on the dual adsorption-catalysis effect of Co-SAs/C_2N with unsaturated coordination structure (Co-N_2 sites) for the redox conversion of LiPS, providing new insights for designing SACs-based hosts with maximized activity in improving the performance of LSBs.

Supporting Information

The supporting information is available free of charge via the Internet at http://pubs.acs.org. The supporting information includes Figure S1-S28 and Table S1-S4 as described in the text, specifically, additional HAADF-STEM, XANES, XRD, XPS, TGA, CV, electrochemical performance, DFT simulation results, and crystal structure.

Corresponding Author

Email: mingxu@mail.buct.edu.cn

Email: david.mitlin2@utexas.edu

Email: guangminzhou@sz.tsinghua.edu.cn

Email: acabot@irec.cat

ACKNOWLEDGMENTS

This work was supported by MCIN/ AEI/10.13039/501100011033/ and by "ERDF A way of making Europe", by the "European Union" through the projects ENE2016- 77798-C4-3-R, and PID2020-116093RB-C43. D. Yang thanks the China Scholarship Council for the scholarship support and the funding from the National Natural Science Foundation of China (NSFC) (Grants No. 22305064). M. Tang and M. Xu thank the financial support by the National Natural Science Foundation of China (Grants 21974007, U1930401, and 22102007). ICN2 acknowledges the support from the Severo Ochoa Programme from Spanish MCIN/AEI (Grant No.: CEX2021-001214-S). ICN2 acknowledges funding from Generalitat de Catalunya 2021SGR00457. This study is part of the Advanced Materials programme and was supported by MCIN with funding from European Union NextGenerationEU (PRTR-C17.I1) and by Generalitat de Catalunya. IREC and ICN2 are both funded by the CERCA Programme/Generalitat de Catalunya. This work was supported by Fundamental Research Funds for the Central Universities (buctrc202112). J. Llorca is a Serra Húnter Fellow and is grateful to projects PID2021-124572OB-C31 and GC2021 SGR 01061 and to ICREA Academia program. This project has received funding from the European Union's Horizon 2020 research and innovation programme under grant agreement No 823717-ESTEEM3. Part of the

present work has been performed in the framework of Universitat Autònoma de Barcelona Materials Science PhD program. The authors are thankful for the support of the BSRF (Beijing Synchrotron Radiation Facility) during the XAFS measurements at the beamline 1W1B, 4B7A, 4B7B, 4B9B, and Shanghai Synchrotron Radiation Facility (SSRF).

REFERENCES

(1) Bruce, P. G.; Freunberger, S. A.; Hardwick, L. J.; Tarascon, J. M. $LigO_2$ and LigS Batteries with High Energy Storage. *Nat. Mater.* **2012**, *11* (1), 19–29.

(2) Zhou, G.; Wang, D. W.; Li, F.; Hou, P. X.; Yin, L.; Liu, C.; Lu, G. Q.; Gentle, I. R.; Cheng, H. M. A Flexible Nanostructured Sulphur-Carbon Nanotube Cathode with High Rate Performance for Li-S Batteries. *Energy Environ. Sci.* **2012**, *5* (10), 8901–8906.

(3) Li, Z.; Guan, B. Y.; Zhang, J.; Lou, X. W. (David). A Compact Nanoconfined Sulfur Cathode for High-Performance Lithium-Sulfur Batteries. *Joule* **2017**, *1* (3), 576–587.

(4) Xiao, Z.; Yang, Z.; Wang, L.; Nie, H.; Zhong, M.; Lai, Q.; Xu, X.; Zhang, L.; Huang, S. A Lightweight TiO2/Graphene Interlayer, Applied as a Highly Effective Polysulfide Absorbent for Fast, Long-Life Lithium-Sulfur Batteries. *Adv. Mater.* **2015**, *27* (18), 2891–2898.

(5) Chen, X.; Peng, H. J.; Zhang, R.; Hou, T. Z.; Huang, J. Q.; Li, B.; Zhang, Q. An Analogous Periodic Law for Strong Anchoring of Polysulfides on Polar Hosts in Lithium Sulfur Batteries: S- or Li-Binding on First-Row Transition-Metal Sulfides? *ACS Energy Lett.* **2017**, *2* (4), 795–801.

(6) Yang, Y.; Zheng, G.; Cui, Y. Nanostructured Sulfur Cathodes. *Chem. Soc. Rev.* **2013**, *42* (7), 3018–3032.

(7) He, J.; Luo, L.; Chen, Y.; Manthiram, A. Yolk–Shelled C@Fe_3O_4 Nanoboxes as Efficient Sulfur Hosts for High-Performance Lithium–Sulfur Batteries. *Adv. Mater.* **2017**, *29* (34), 1702707.

(8) Sun, Z.; Zhang, J.; Yin, L.; Hu, G.; Fang, R.; Cheng, H. M.; Li, F. Conductive Porous Vanadium Nitride/Graphene Composite as Chemical Anchor of Polysulfides for Lithium-Sulfur Batteries. *Nat. Commun.* **2017**, *8*, 14627.

(9) Li, G.; Lei, W.; Luo, D.; Deng, Y.; Deng, Z.; Wang, D.; Yu, A.; Chen, Z. Stringed "Tube on Cube" Nanohybrids as Compact Cathode Matrix for High-Loading and Lean-Electrolyte Lithium-Sulfur Batteries. *Energy Environ. Sci.* **2018**, *11* (9), 2372–2381.

(10) Zhang, L.; Liu, D.; Muhammad, Z.; Wan, F.; Xie, W.; Wang, Y.; Song, L.; Niu, Z.; Chen, J. Single Nickel Atoms on Nitrogen-Doped Graphene Enabling Enhanced Kinetics of Lithium–Sulfur Batteries. *Adv. Mater.* **2019**, *31* (40), 1903955.

(11) Liu, J.; Yuan, L.; Yuan, K.; Li, Z.; Hao, Z.; Yang, J.; Huang, Y. SnO2 as a high-efficiency polysulfide trap in lithium-sulfur batteries. *Nanoscale.* **2016**, *8* (8), 13638.

(12) Yang, D.; Liang, Z.; Zhang, C.; Biendicho, J. J.; Botifoll, M.; Spadaro, M. C.; Chen, Q.; Li, M.; Ramon, A.; Moghaddam, A. O.; Llorca, J.; Wang, J.; Morante, J. R.; Arbiol, J.; Chou, S. L.; Cabot, A. $NbSe_2$ Meets C_2N: A 2D-2D Heterostructure Catalysts as Multifunctional Polysulfide Mediator in Ultra-Long-Life Lithium–Sulfur Batteries. *Adv. Energy Mater.* **2021**, *11* (36), 2101250.

(13) Zhou, T.; Lv, W.; Li, J.; Zhou, G.; Zhao, Y.; Fan, S.; Liu, B.; Li, B.; Kang, F.; Yang, Q. H. Twinborn TiO_2-TiN Heterostructures Enabling Smooth Trapping-Diffusion-Conversion of Polysulfides towards Ultralong Life Lithium-Sulfur Batteries. *Energy Environ. Sci.* **2017**, *10* (7), 1694–1703.

(14) Liu, K.; Fu, J.; Lin, Y.; Luo, T.; Ni, G.; Li, H.; Lin, Z.; Liu, M. Insights into the Activity of Single-Atom Fe-N-C Catalysts for Oxygen Reduction Reaction. *Nat. Commun.* **2022**, *13* (1), 1–8.

(15) Zhang, Y.; Liu, J.; Wang, J.; Zhao, Y.; Luo, D.; Yu, A.; Wang, X.; Chen, Z. Engineering Oversaturated Fe-N 5 Multifunctional Catalytic Sites for Durable Lithium-Sulfur Batteries . *Angew. Chem., Int. Ed.* **2021**, *133* (51), 26826–26833.

(16) Zhang, X.; Yang, T.; Zhang, Y.; Wang, X.; Wang, J.; Li, Y.; Yu, A.; Wang, X.; Chen, Z. Single Zinc Atom Aggregates: Synergetic Interaction to Boost Fast Polysulfide Conversion in Lithium-Sulfur Batteries. *Adv. Mater.* **2023**, *35* (6), 2208470.

(17) Wang, J.; Qiu, W.; Li, G.; Liu, J.; Luo, D.; Zhang, Y.; Zhao, Y.; Zhou, G.; Shui, L.; Wang, X.; Chen, Z. Coordinatively Deficient Single-Atom Fe-N-C Electrocatalyst with Optimized Electronic Structure for High-Performance Lithium-Sulfur Batteries. *Energy Storage Mater.* **2022**, *46*, 269–277.

(18) Han, Z.; Zhao, S.; Xiao, J.; Zhong, X.; Sheng, J.; Lv, W.; Zhang, Q.; Zhou, G.; Cheng, H. M. Engineering D-p Orbital Hybridization in Single-Atom Metal-Embedded Three-Dimensional Electrodes for Li–S Batteries. *Adv. Mater.* **2021**, *33* (44), 2105947.

(19) Qiu, Y.; Fan, L.; Wang, M.; Yin, X.; Wu, X.; Sun, X.; Tian, D.; Guan, B.; Tang, D.; Zhang, N. Precise Synthesis of Fe-N_2 sites with High Activity and Stability for Long-Life Lithium-Sulfur Batteries. *ACS Nano* **2020**, *14* (11), 16105–16113.

(20) Volosskiy, B.; Li, M.; Zhao, Z.; Wang, Y.; Sun, H.; An, P.; Chen, W.; Guo, Z.; Lee, C.; Chen, D.; Shakir, I.; Liu, M.; Hu, T.; Li, Y.; Kirkland, A. I.; Duan, X.; Huang, Y. General Synthesis and Definitive Structural Identification of MN_4C_4 Single-Atom Catalysts with Tunable Electrocatalytic Activities. *Nat. Catal.* **2018**, *1* (1), 63–72.

(21) Chen, Y.; Ji, S.; Chen, C.; Peng, Q.; Wang, D.; Li, Y. Single-Atom Catalysts: Synthetic Strategies and Electrochemical Applications. *Joule* **2018**, *2* (7), 1242–1264.

(22) Chen, K.; Liu, K.; An, P.; Li, H.; Lin, Y.; Hu, J.; Jia, C.; Fu, J.; Li, H.; Liu, H.; Lin, Z.; Li, W.; Li, J.; Lu, Y. R.; Chan, T. S.; Zhang, N.; Liu, M. Iron Phthalocyanine with Coordination Induced Electronic Localization to Boost Oxygen Reduction Reaction. *Nat. Commun.* **2020**, *11* (1), 1–8.

(23) Ding, Y.; Cheng, Q.; Wu, J.; Yan, T.; Shi, Z.; Wang, M.; Yang, D.; Wang, P.; Zhang, L.; Sun, J. Enhanced Dual-Directional Sulfur Redox via a Biotemplated Single-Atomic Fe–N_2 Mediator Promises Durable Li–S Batteries. *Adv. Mater.* **2022**, *34* (28), 2202256.

(24) Zhong, W.; Qiu, Y.; Shen, H.; Wang, X.; Yuan, J.; Jia, C.; Bi, S.; Jiang, J. Electronic Spin Moment As a Catalytic Descriptor for Fe Single-Atom Catalysts Supported on C_2N. *J. Am. Chem. Soc.* **2021**, *143* (11), 4405–4413.

(25) Lin, C.; Zhang, H.; Song, X.; Kim, D. H.; Li, X.; Jiang, Z.; Lee, J. H. 2D-Organic Framework Confined Metal Single Atoms with the Loading Reaching the Theoretical Limit. *Mater. Horizons* **2020**, *7* (10), 2726–2733.

(26) Xu, J.; Mahmood, J.; Dou, Y.; Dou, S.; Li, F.; Dai, L.; Baek, J. B. 2D Frameworks of C_2N and C_3N as New Anode Materials for Lithium-Ion Batteries. *Adv. Mater.* **2017**, *29* (34), 1702007.

(27) Liang, Z.; Yang, D.; Tang, P.; Zhang, C.; Jacas Biendicho, J.; Zhang, Y.; Llorca, J.; Wang, X.; Li, J.; Heggen, M.; David, J.; Dunin-Borkowski, R. E.; Zhou, Y.; Morante, J. R.; Cabot, A.; Arbiol, J. Atomically Dispersed Fe in a C_2N Based Catalyst as a Sulfur Host for Efficient Lithium–Sulfur Batteries. *Adv. Energy Mater.* **2021**, *11* (5), 2003507.

(28) Chu, C.; Zhu, Q.; Pan, Z.; Gupta, S.; Huang, D.; Du, Y.; Weon, S.; Wu, Y.; Muhich, C.; Stavitski, E.; Domen, K.; Kim, J. H. Spatially Separating Redox Centers on 2D Carbon Nitride with Cobalt Single Atom for Photocatalytic H_2O_2 Production. *Proc. Natl. Acad. Sci. USA* **2020**, *117* (12), 6376–6382.

(29) Shen, T.; Huang, X.; Xi, S.; Li, W.; Sun, S.; Hou, Y. The ORR Electron Transfer Kinetics Control via Co-N_x and Graphitic N Sites in Cobalt Single Atom Catalysts in Alkaline and Acidic Media. *J. Energy Chem.* **2022**, *68*, 184–194.

(30) Lu, Q.; Wu, H.; Zheng, X.; Chen, Y.; Rogach, A. L.; Han, X.; Deng, Y.; Hu, W. Encapsulating Cobalt Nanoparticles in Interconnected N-Doped Hollow Carbon Nanofibers with Enriched Co-N-C Moiety for Enhanced Oxygen Electrocatalysis in Zn-Air Batteries. *Adv. Sci.* **2021**, *8* (20), 2101438.

(31) Pei, Z.; Lu, X. F.; Zhang, H.; Li, Y.; Luan, D.; Lou, X. W. (David). Highly Efficient Electrocatalytic Oxygen Evolution Over Atomically Dispersed Synergistic Ni/Co Dual Sites. *Angew. Chem., Int. Ed.* **2022**, *134* (40), e202207537.

(32) Yao. Y.; Huang, Z.; Xie, P.; Wu, L.; Ma, L.; Li, T.; Pang, Z.; Jiao, M.; Liang, Z.; Gao, J.; He, Y.; Kline, D. J.; Zachariah, M. R.; Wang, C.; Lu, J; Wu, T.; Li, T.; Wang, C.; Shahbazian-Yassar, R.; Hu, L. High temperature shockwave stabilized single atoms. *Nat. Nanotechnol.* **2019**, *14*, 851 – 857.

(33) Ding, K.; Hu, J.; Luo, J.; Zhao, L.; Jin, W.; Liu, Y.; Wu, Z.; Zou, G.; Hou, H.; Ji, X. Robust Electronic Correlation of Co-CoN_4 Hybrid Active Sites for Durable Rechargeable Zn-Air Batteries. *Adv. Funct. Mater.* **2022**, *32* (52), 2207331.

(34) Du, Z.; Chen, X.; Hu, W.; Chuang, C.; Xie, S.; Hu, A.; Yan, W.; Kong, X.; Wu, X.; Ji, H.; Wan, L. J. Cobalt in Nitrogen-Doped Graphene as Single-Atom Catalyst for High-Sulfur Content Lithium-Sulfur Batteries. *J. Am. Chem. Soc.* **2019**, *141* (9), 3977–3985.

(35) Shi, W.; Li, Z.; Gao, Z.; Liang, Z.; Liu, H.; Han, Y. C.; Niu, H.; Song, B.; Chi, X.; Zhou, J.; Wang, H.; Xia, B.; Yao, Y.; Tian, Z.-Q. Transient and general synthesis of high-density and ultrasmall nanoparticles on two-dimensional porous carbon via coordinated carbothermal shock. *Nat. Commun.* 2023, 14, 2294.

(36) Wang, Z.; Jin, X.; Zhu, C.; Liu, Y.; Tan, H.; Ku, R.; Zhang, Y.; Zhou, L.; Liu, Z.; Hwang, S. J.; Fan, H. J. Atomically Dispersed Co_2–N_6 and Fe–N_4 Costructures Boost Oxygen Reduction Reaction in Both Alkaline and Acidic Media. *Adv. Mater.* **2021**, *33* (49), 2104718.

(37) Wang, L.; Ni, Y.; Hou, X.; Chen, L.; Li, F.; Chen, J. A Two-Dimensional Metal–Organic Polymer Enabled by Robust Nickel–Nitrogen and Hydrogen Bonds for Exceptional Sodium-Ion Storage. *Angew. Chem., Int. Ed.* **2020**, *59* (49), 22126–22131.

(38) Yang, D.; Zhang, C.; Biendicho, J. J.; Han, X.; Liang, Z.; Du, R.; Li, M.; Li, J.; Arbiol, J.; Llorca, J.; Zhou, Y.; Morante, J. R.; Cabot, A. ZnSe/N-Doped Carbon Nanoreactor

with Ultiple Adsorption Sites for Stable Lithium−Sulfur Batteries. *ACS Nano* **2020**, *14* (11), 15492–15504.

(39) Song, J.; Yu, Z.; Gordin, M. L.; Wang, D. Advanced Sulfur Cathode Enabled by Highly Crumpled Nitrogen Doped Graphene Sheets for High-Energy-Density Lithium-Sulfur Batteries. *Nano Lett.* **2016**, *16*, 864–870.

(40) Song, Y.; Zou, L.; Wei, C.; Zhou, Y.; Hu, Y. Single-Atom Electrocatalysts for Lithium–Sulfur Chemistry: Design Principle, Mechanism, and Outlook. *Carbon Energy* **2022**, *5*, e286.

(41) Liang, Z.; Shen, J.; Xu, X.; Li, F.; Liu, J.; Yuan, B.; Yu, Y.; Zhu, M. Advances in the Development of Single-Atom Catalysts for High-Energy-Density Lithium–Sulfur Batteries. *Adv. Mater.* **2022**, *34* (30), 2200102.

(42) Pang, Q.; Tang, J.; Huang, H.; Liang, X.; Hart, C.; Tam, K. C.; Nazar, L. F. A Nitrogen and Sulfur Dual-Doped Carbon Derived from Polyrhodanine@Cellulose for Advanced Lithium-Sulfur Batteries. *Adv. Mater.* **2015**, *27* (39), 6021–6028.

(43) Zhang, C.; Du, R.; Biendicho, J. J.; Yi, M.; Xiao, K.; Yang, D.; Zhang, T.; Wang, X.; Arbiol, J.; Llorca, J.; Zhou, Y.; Morante, J. R.; Cabot, A. Tubular CoFeP@CN as a Mott-Schottky Catalyst with Multiple Adsorption Sites for Robust Lithium-Sulfur Batteries. *Adv. Energy Mater.* **2021**, *11*, 2100432.

(44) Zheng, J.; Tian, J.; Wu, D.; Gu, M.; Xu, W.; Wang, C.; Gao, F.; Engelhard, M. H.; Jiguang, Z.; Liu, J.; Xiao, J. Lewis Acid-Base Interactions between Polysulfides and Metal Organic Framework in Lithium Sulfur Batteries. *Nano Lett.* **2014**, *14*, 2345–2352.

(45) Zhou, G.; Zhou, G.; Yang, A.; Gao, G.; Yu, X.; Xu, J.; Liu, C.; Ye, Y.; Pei, A.; Wu, Y.; Peng, Y.; Li, Y.; Liang, Z.; Liu, K.; Wang, L. W.; Cui, Y.; Cui, Y. Supercooled Liquid Sulfur Maintained in Three-Dimensional Current Collector for High-Performance Li-S Batteries. *Sci. Adv.* **2020**, *6* (21), eaay5098.

(46) Li, C.; Qi, S.; Zhu, L.; Zhao, Y.; Huang, R.; He, Y.; Ge, W.; Liu, X.; Zhao, M.; Xu, L.; Qian, Y. Regulating Polysulfide Intermediates by Ultrathin Co-Bi Nanosheet Electrocatalyst in Lithium-Sulfur Batteries. *Nano Today* **2021**, *40*, 101246.

(47) Lin, H.; Yang, L.; Jiang, X.; Li, G.; Zhang, T.; Yao, Q.; Zheng, G. W.; Lee, J. Y. Electrocatalysis of Polysulfide Conversion by Sulfur-Deficient MoS_2 Nanoflakes for Lithium-Sulfur Batteries. *Energy Environ. Sci.* **2017**, *10* (6), 1476–1486.

(48) Yang, D.; Liang, Z.; Tang, P.; Zhang, C.; Tang, M.; Li, Q.; Biendicho, J. J.; Li, J.; Heggen, M.; Dunin-Borkowski, R. E.; Xu, M.; Llorca, J.; Arbiol, J.; Morante, J. R.; Chou, S. L.; Cabot, A. A High Conductivity 1D π–d Conjugated Metal–Organic Framework with Efficient Polysulfide Trapping-Diffusion-Catalysis in Lithium–Sulfur Batteries. *Adv. Mater.* **2022**, *34* (10), 2108835.

(49) Moy, D.; Manivannan, A.; Narayanan, S. R. Direct Measurement of Polysulfide Shuttle Current: A Window into Understanding the Performance of Lithium-Sulfur Cells. *J. Electrochem. Soc.* **2015**, *162* (1), A1–A7.

(50) Chen, Y.; Zhang, W.; Zhou, D.; Tian, H.; Su, D.; Wang, C.; Stockdale, D.; Kang, F.; Li, B.; Wang, G. Co-Fe Mixed Metal Phosphide Nanocubes with Highly Interconnected-Pore Architecture as an Efficient Polysulfide Mediator for Lithium-Sulfur Batteries. *ASC nano* **2019**, *13*, 4731–4741.

(51) Yuan, Z.; Peng, H.; Hou, T.; Huang, J.; Chen, C.; Wang, D.; Cheng, X.; Wei, F.; Zhang, Q. Powering Lithium−Sulfur Battery Performance by Propelling Polysulfide Redox at Sulfiphilic Hosts. *Nano Lett.* **2016**, *16*, 519–527.

(52) Zhou, G.; Tian, H.; Jin, Y.; Tao, X.; Liu, B.; Zhang, R.; Seh, Z.; Zhou, D.; Liu, Y.; Sun, J.; Zhao, J.; Zu, C.; Wu, D. S.; Zhang, Q.; Cui, Y. Catalytic Oxidation of Li_2S on the Surface of Metal Sulfides for Li−S Batteries. *Proc. Natl. Acad. Sci. USA* **2016**, *114* (5), 840–845.

(53) Zhu, X.; Zhao, W.; Song, Y.; Li, Q.; Ding, F.; Sun, J.; Zhang, L.; Liu, Z. In Situ Assembly of 2D Conductive Vanadium Disulfide with Graphene as a High-Sulfur-Loading Host for Lithium–Sulfur Batteries. *Adv. Energy Mater.* **2018**, *8* (20), 1800201.

(54) Li, M.; Yang, D.; Biendicho, J. J.; Han, X.; Zhang, C.; Liu, K.; Diao, J.; Li, J.; Wang, J.; Heggen, M.; Dunin-Borkowski, R. E.; Wang, J.; Henkelman, G.; Morante, J. R.; Arbiol, J.; Chou, S. L.; Cabot, A. Enhanced Polysulfide Conversion with Highly Conductive and Electrocatalytic Iodine-Doped Bismuth Selenide Nanosheets in Lithium–Sulfur Batteries. *Adv. Funct. Mater.* **2022**, *32* (26), 2200529.

(55) Du, M.; Geng, P.; Pei, C.; Jiang, X.; Shan, Y.; Hu, W.; Ni, L.; Pang, H. High-Entropy Prussian Blue Analogues and Their Oxide Family as Sulfur Hosts for Lithium-Sulfur Batteries. *Angew. Chem., Int. Ed.* **2022**, *134* (41), e202209350.

(56) Xiao, R.; Yu, T.; Yang, S.; Chen, K.; Li, Z.; Liu, Z.; Hu, T.; Hu, G.; Li, J.; Cheng, H. M.; Sun, Z.; Li, F. Electronic Structure Adjustment of Lithium Sulfide by a Single-Atom Copper Catalyst toward High-Rate Lithium-Sulfur Batteries. *Energy Storage Mater.* **2022**, *51*, 890–899.

(57) Eftekhari, A. Energy Efficiency: A Critically Important but Neglected Factor in Battery Research. *Sustain. Energy Fuels* **2017**, *1* (10), 2053–2060.

(58) Tian, Y.; Li, G.; Zhang, Y.; Luo, D.; Wang, X.; Zhao, Y.; Liu, H.; Ji, P.; Du, X.; Li, J.; Chen, Z. Low-Bandgap Se-Deficient Antimony Selenide as a Multifunctional Polysulfide Barrier toward High-Performance Lithium–Sulfur Batteries. *Adv. Mater.* **2020**, *32* (4), 1904876.

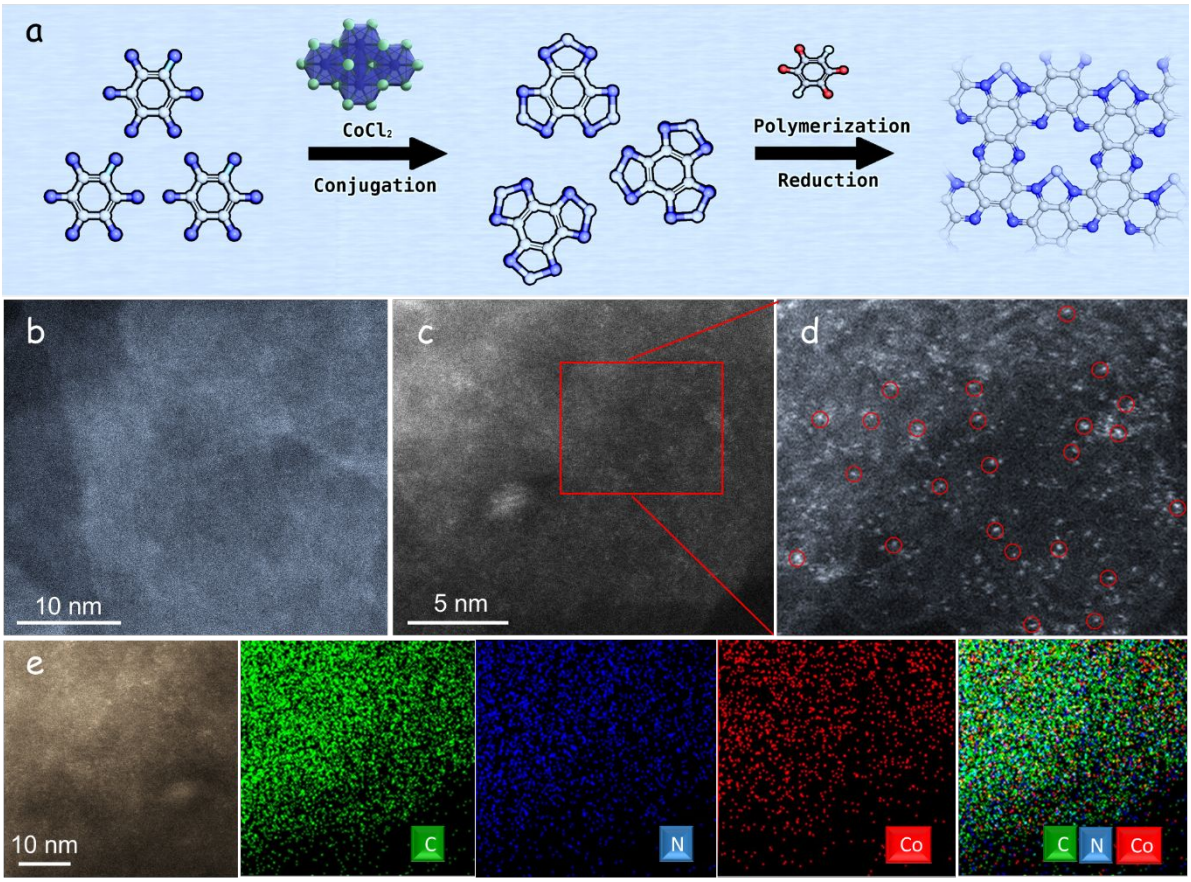

Figure 1. (a) Schematic illustration of the synthesis of Co single atoms supported by C_2N (Co-SAs/C_2N). (dark blue = nitrogen, light gray = carbon, red = oxygen, light green = chlorine, and light blue = cobalt). (b-d) HAADF-STEM images at different magnifications of Co-SAs/C_2N. Red circles display single Co atoms shown as bright contrast spots. (e) HAADF-STEM image and corresponding EDX mapping showing the elemental distribution of Co-SAs/C_2N.

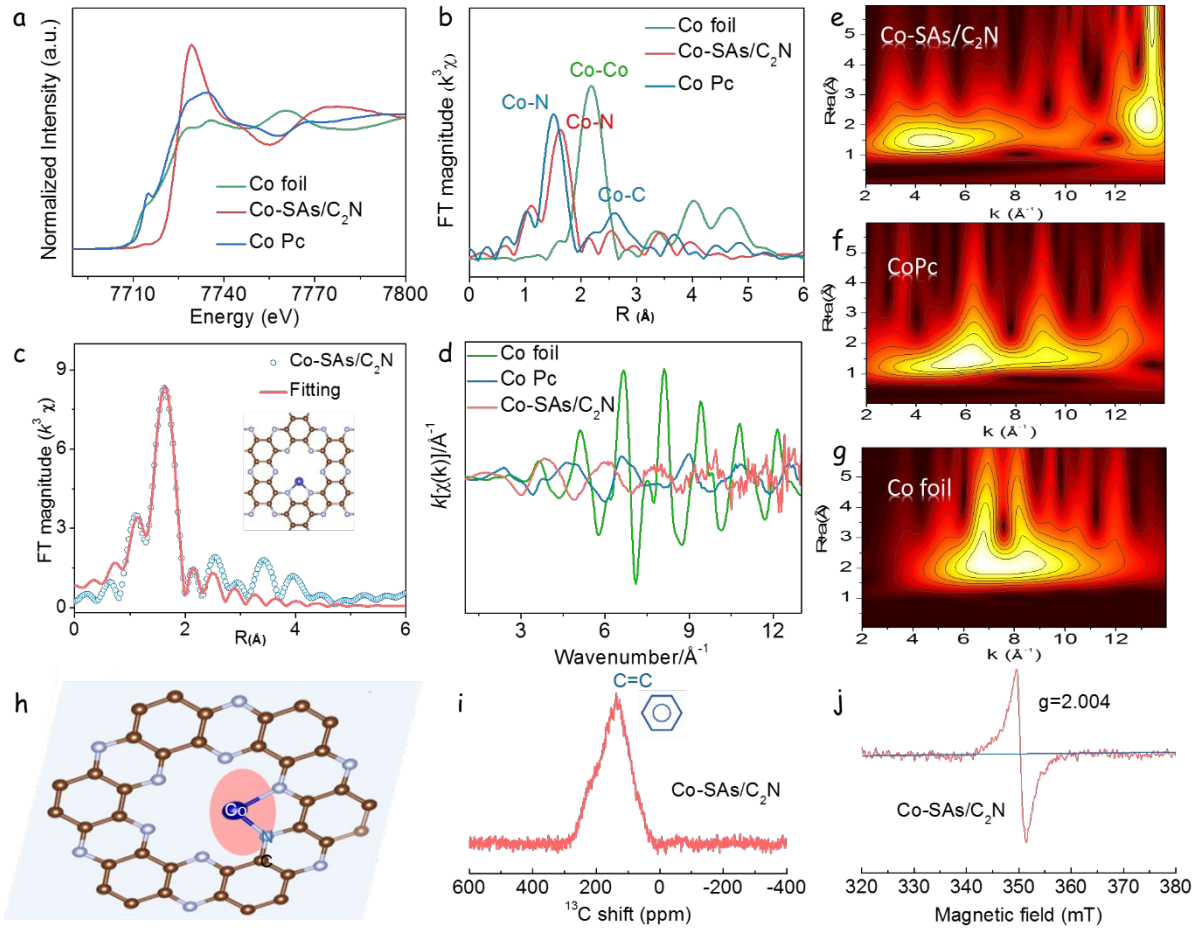

Figure 2. (a) XANES spectra of Co-SAs/C_2N, CoPc, and Co foil. (b) Co K-edge FT-EXAFS spectra in R space of Co-SAs/C_2N, CoPc, and Co foil. (c) EXAFS fitting curves in R space for the Co-SAs/C_2N sample (inset is the top view of the optimized stable Co-N_2 coordinated structure). (d) EXAFS oscillations of Co-SAs/C_2N with respect to the reference samples. (e-g) Wavelet transformed contour plots at Co K-edge of Co-SAs/C_2N, CoPc, and Co foil. (h) The atomic structure model of the Co-SAs/C_2N. (i) Solid state ^{13}C MAS-NMR spectrum for Co-SAs/C_2N. (j) CW-EPR spectrum of Co-SAs/C_2N, with a g-factor of 2.004.

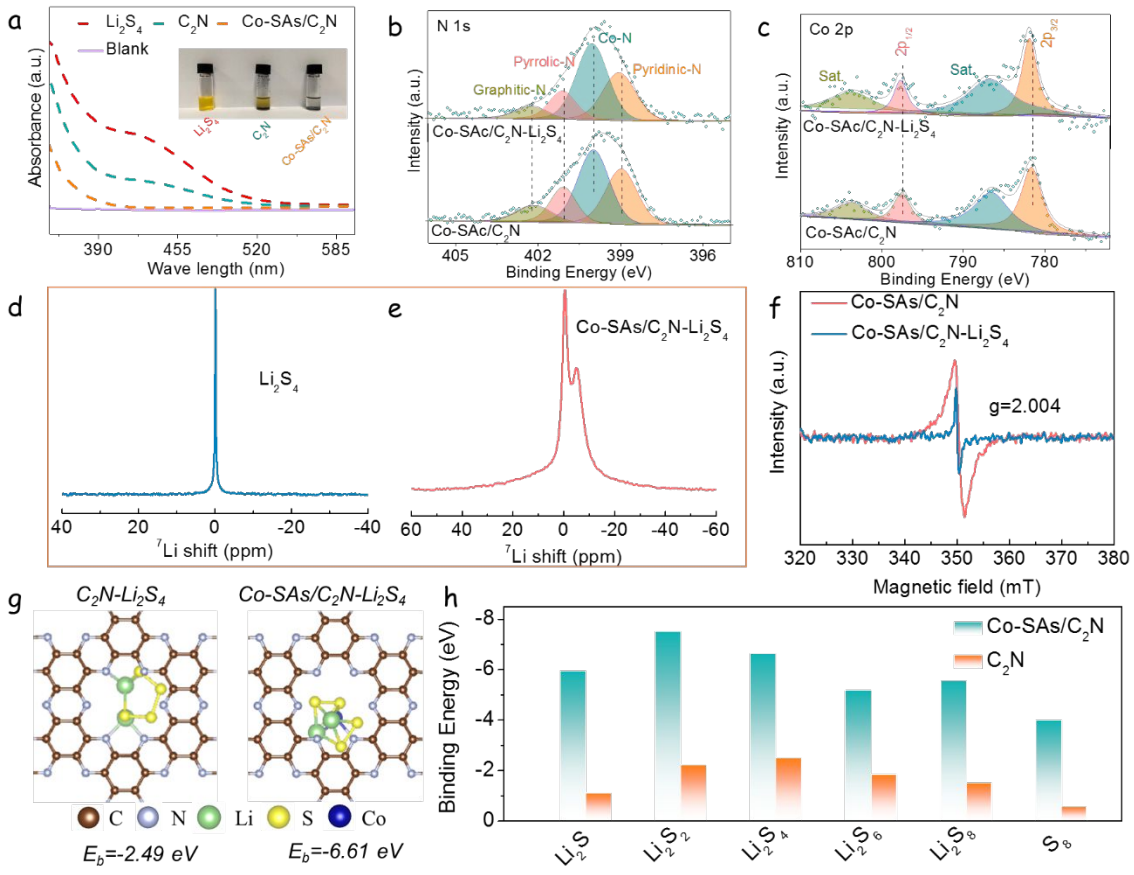

Figure 3. (a) UV-Vis spectra and optical photograph of the flasks containing a Li_2S_4 solution and the different materials after overnight adsorption. (b) High-resolution N 1s XPS spectra and (c) high-resolution Co 2p XPS spectra of Co-SAs/C_2N before and after Li_2S_4 adsorption. Solid-state ^7Li NMR spectrum of (d) Li_2S_4 and (e) Co-SAs/C_2N-Li_2S_4. (f) CW-EPR spectrum for Co-SAs/C_2N and Co-SAs/C_2N-Li_2S_4. (g) Relaxed Li_2S_4-adsorbed structure on the surface of C_2N and Co-SAs/C_2N calculated with DFT. (h) Binding energies between LiPS species (Li_2S, Li_2S_2, Li_2S_4, Li_2S_6, Li_2S_8 and S_8) and C_2N or Co-SAs/C_2N as calculated by DFT.

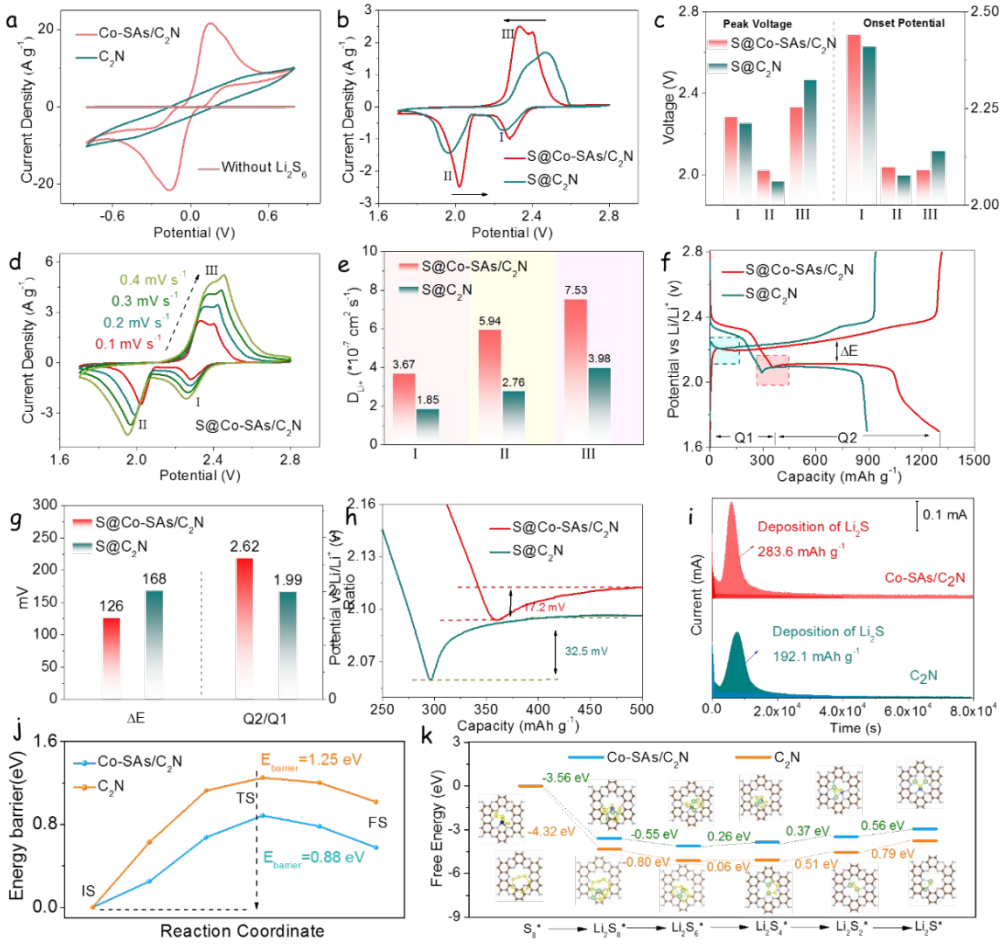

Figure 4. (a) CV profiles of symmetric cells with Co-SAs/C_2N and C_2N host materials in an electrolyte containing 0.5 mol L^{-1} Li_2S_6 and 1 mol L^{-1} LiTFSI dissolved in DOL/DME (v/v = 1/1). (b) CV profiles of Li-S coin cells at a scan rate of 0.1 mV s^{-1}. (c) Peak voltages and onset potentials of Li-S cells based on the CV curves. (d) CV profile of the S@Co-SAs/C_2N electrode with scan rates ranging from 0.1-0.5 mV s^{-1}. (e) Li^+ diffusion coefficient of S@Co-SAs/C_2N and S@C_2N electrodes calculated from I, II, and III. (f) Galvanostatic charge/discharge profiles of various electrodes with a 0.1 C current rate. (g) Values of ΔE and Q2/Q1 obtained from charge/discharge profiles. (h) Discharge curves of S@Co-SAs/C_2N and S@C_2N electrodes exhibiting the overpotentials for the transformation from soluble LiPS to insoluble Li_2S_2/Li_2S. (i) Potentiostatic discharge profile at 2.05 V on S@Co-SAs/C_2N and S@C_2N electrodes with Li_2S_8 catholyte to evaluate the nucleation kinetics of Li_2S. (j) Decomposition energy barriers of Li_2S on C_2N and Co-SAs/C_2N for different adsorbate configurations. (k) Gibbs free energy profiles and adsorption conformation of LiPS species on the surface of C_2N and Co-SAs/C_2N.

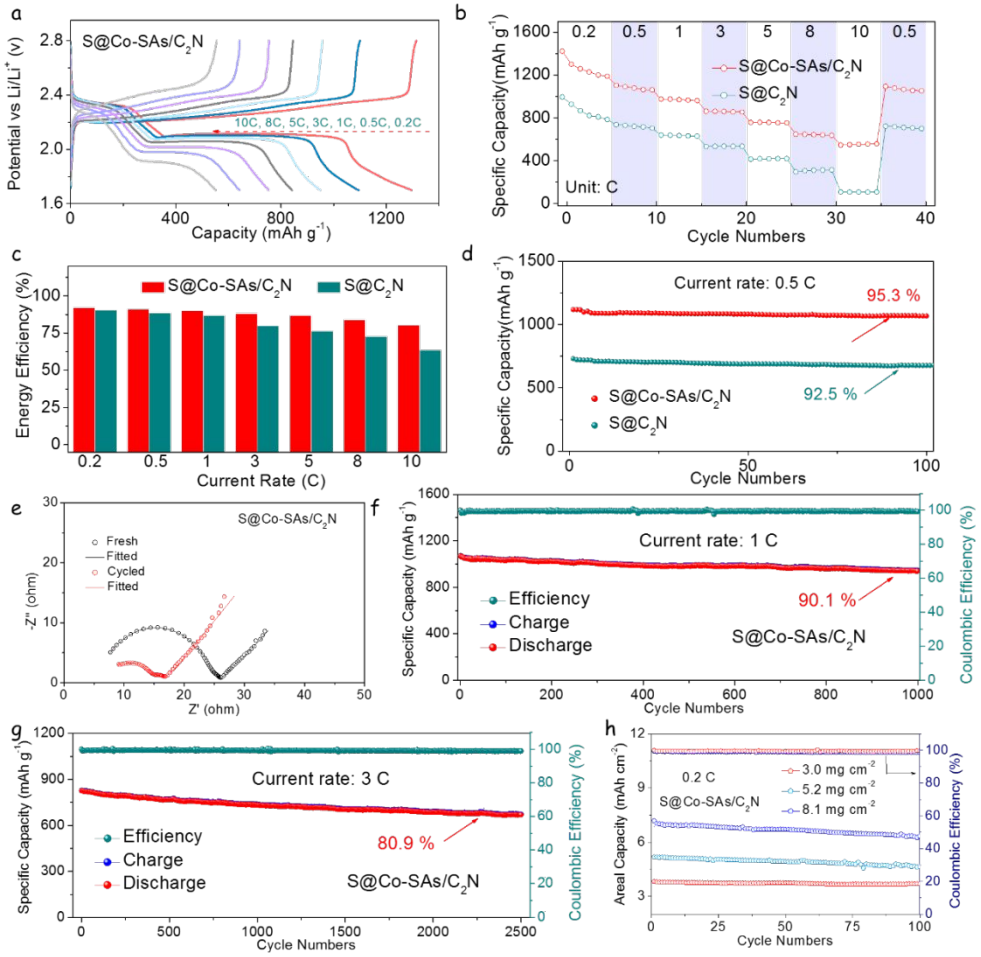

Figure 5. Electrochemical performance of Li-S coin cells. (a) Galvanostatic charge/discharge profile of S@Co-SAs/C_2N electrodes at various rates from 0.2 C to 10 C. (b) Rate capabilities of the S@Co-SAs/C_2N and S@C_2N electrodes at different current rates. (c) Energy efficiency of two different electrodes at various current rates. (d) Capacity retention of S@Co-SAs/C_2N and S@C_2N electrodes at 0.5 C over 100 cycles. (e) Nyquist plot of EIS data from S@Co-SAs/C_2N electrodes before and after cycling at 0.5 C. (f) Cycling stability of S@Co-SAs/C_2N electrodes at 1 C over 1000 cycles. (g) Ultra-long cycling test of the S@Co-SAs/C_2N electrode at 3 C over 2500 cycles. (h) High-loading cycling performances with sulfur loadings of 3.0, 5.2, and 8.1 mg cm^{-2} at 0.2 C of S@Co-SAs/C_2N electrodes.

Abstract Graphics